Available online at www.sciencedirect.com

SciVerse ScienceDirect

journal homepage: www.elsevier.com/locate/he

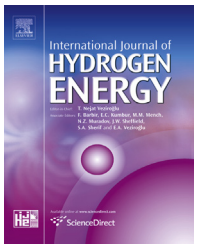

Degradation phenomena in PEM fuel cell with dead-ended anode

Toyoaki Matsuura, Jixin Chen, Jason B. Siegel, Anna G. Stefanopoulou*

Department of Mechanical Engineering, University of Michigan, 2350 Hayward St., Ann Arbor, MI 48109, USA

ARTICLE INFO

Article history:
Received 25 March 2013
Received in revised form
14 June 2013
Accepted 22 June 2013
Available online 22 July 2013

Keywords:
Fuel cell degradation
Dead-ended anode
Carbon corrosion
Membrane pin-hole

ABSTRACT

To improve the performance and durability of a dead-ended anode (DEA) fuel cell, it is important to understand and characterize the degradation associated with the DEA operation. To this end, the multiple degradation phenomena in DEA operation were investigated via systematic experiments. Three lifetime degradation tests were conducted with different cell temperatures and cathode relative humidities, during which the temporal evolutions of cell voltage and high frequency resistance (HFR) were recorded. When the cathode supply was fully humidified and the cell temperature was mild, the cathode carbon corrosion was the predominant degradation observed from scanning electronic microscopy (SEM) of postmortem samples. The catalyst layer and membrane thickness were measured at multiple locations across the cell active area in order to map the degradation patterns. These observations confirm a strong correlation between the cathode carbon corrosion and the anode fuel starvation occurring near the cell outlet. When the cathode supply RH reduced to 50%, membrane pin-hole failures terminated the degradation test. Postmortem analysis showed membrane cracks and delamination in the inlet region where membrane water content was the lowest.

1. Introduction

To meet the Department of Energy (DOE) target of 30 $/kW for automotive application by 2015 [1], cost reduction in both fuel cell components and balance of plant (BOP) accessories is critical. There are innovations in fuel cell components such as low Pt loading or non-precious metal catalysts and hydrocarbon electrolyte membranes, which reduce the cost while maintaining the performance [2–7]. Additionally, cost reduction in BOP components, which currently accounts for around 50% of the fuel cell system cost, is also essential [1].

Conventional fuel cell systems for automotive applications employ a flow-through anode (FTA) mode which requires an additional fuel recirculation subsystem to increase efficiency of hydrogen usage [1,8]. The anode recirculation subsystems, including water separator and ejector/blower, require hydrogen grade plumbing. These accessories add system volume, weight and cost.

In contrast to the FTA mode, the DEA operation relies on pressure regulation rather than mass flow control to supply the hydrogen necessary to maintain the electrochemical reaction [9,10]. Although periodic purging is required to remove the accumulated nitrogen and water, in the anode high utilization of hydrogen with unity stoichiometry ratio can be achieved [11]. Moreover, the anode subsystem can be simplified by removing the water separator and ejector/blower and the overall system cost can be reduced.

* *Corresponding author.*
E-mail address: jixinc@umich.edu (J. Chen).

0360-3199/$ – see front matter
http://dx.doi.org/10.1016/j.ijhydene.2013.06.096

Between consecutive purges, however, nitrogen and water from cathode crossover gradually accumulate in the DEA [12,13], leading to local hydrogen depletion or starvation and associated voltage decay with time. One primary concern in DEA operation is the cathode carbon corrosion due to the fuel starvation in the anode [14–17]. In our recent work [18] the carbon corrosion and associated irreversible voltage loss in DEA operation have been studied by simulation. In addition to the catalyst layer degradation, membrane deformation also occurs in DEA operation particularly in the channel inlet region that experiences the driest conditions, as observed in our preliminary experiments [19] and verified in this more extensive study.

It is therefore of interest to investigate the degradation phenomena in DEA operation with systematic experiments to determine the impacts from the key operating parameters. Once the degradation is characterized and correctly quantified, we can determine whether the benefit of reduced system cost is offset by more stringent durability concerns for DEA systems, and then develop strategies to mitigate the degradation while maintaining the simplified system architecture. We ultimately anticipate to develop DEA fuel cell systems with reduced cost as well as reasonable power density and durability. This paper represents a step towards the goal.

2. Experimental conditions

The lifetime degradation tests are designed to operate the cell in DEA mode under typical operating conditions and reasonable current load, with periodic evaluations performed under flow-through conditions. The typical voltage cycling behavior under galvanostatic DEA mode with periodic purges is shown in Fig. 2 in Subsection 2.2. The detailed experimental conditions for three cases are reported in Subsection 2.3. The experimental results from the three cases will be discussed in Section 3.

2.1. Experimental setup

A 50 cm^2 active area cell was used for each of the degradation tests in this paper. The MEA consists of two 400 μm thickness (before compression) carbon papers with micro porous layers (MPL, SIGRACET 10BC, SGL), and catalyst coated membrane (CCM, Ion Power) with 25 μm-thick membrane (Nafion, Dupont) and 0.3 mg cm^{-2} Pt loading at both anode and cathode. The platinum/carbon weight percentage (wt%) was not released by the company.

There are twenty five parallel straight gas channels (7.3 cm length, 1.78 mm depth and 2.08 mm width) in the anode, and five parallel semi-serpentine channels (0.69 mm width and 0.99 mm depth) in the cathode. The flow pathway in the anode is perpendicular to that in the cathode while the cell was placed with a 45° to the horizontal plane and maintained a co-flow configuration. A 45 W heater is attached to the end plates for both anode and cathode to maintain uniform cell temperature.

A schematic of the experimental setup is shown in Fig. 1. Humidified air and hydrogen are controlled by mass flow controllers to feed into the fuel cell in FTA mode. In DEA operation, dry hydrogen is supplied to the anode while the cathode is still fed with humidified flow-through air. The direction of hydrogen flow in the anode is indicated by the arrows in Fig. 1. The temperature of the cathode humidifier, or dew point, is controlled to achieve the desired cathode inlet RH. The anode pressure is regulated upstream in DEA operation whereas the cathode pressure is controlled by a back pressure regulator. There is a solenoid valve at the downstream of the anode to perform scheduled purge. The purge interval is 900 ms during which the turbulent orifice flow clears the accumulated nitrogen and water in the anode channel end. After the degradation test, the aged MEA was cut

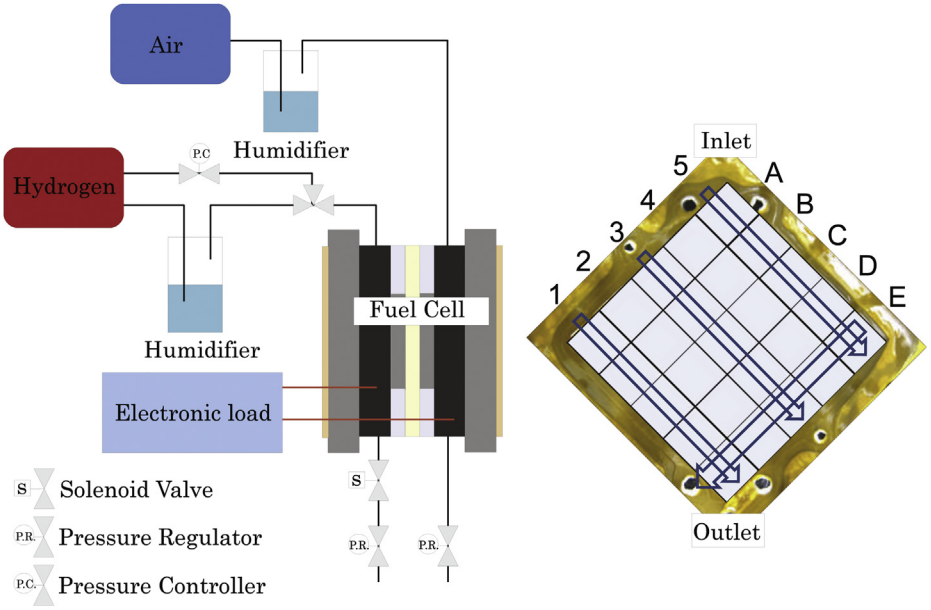

Fig. 1 – Schematic of the experimental setup. The arrows indicate the direction of hydrogen flow.

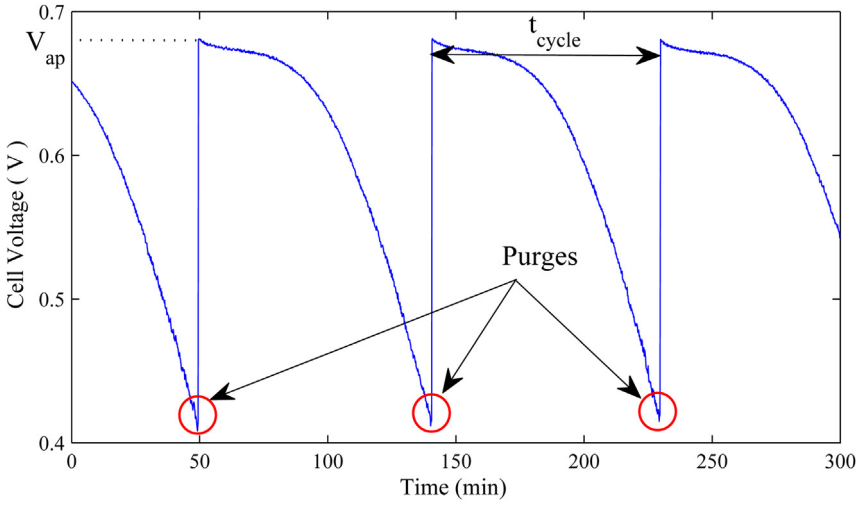

Fig. 2 – Typical voltage evolution in DEA operation. These purge cycles are observed with 0.4 A cm^{-2} current density, 60 °C cell temperature, 100% cathode RH, 2.5 cathode stoichiometry and 4.0 psig anode/cathode pressure.

into 25 pieces (1 × 1 cm^2 for each) to observe the cross section morphology using a Scanning Electron Microscope (SEM, Quanta, FEI). The 25 pieces of sample correspond to the 5 × 5 grids in Fig. 1.

2.2. *Typical voltage behavior*

Fig. 2 shows the typical voltage evolution with time during galvanostatic DEA operation. The gradual and reversible voltage drop after every purge is predominantly caused by nitrogen accumulation in the anode [12], although water also contributes. The voltage is recovered by a scheduled purge. At fixed current, pressure, temperature, cathode RH and stoichiometry ratio, the cell reaches a repeatable voltage pattern in between purges. This repeatable voltage pattern is defined as a cycle in DEA operation. The cell voltage right after purge is defined as V_{ap} in this paper, and the amount of time between two consecutive purges is defined as t_{cycle}. In the degradation test, the purge is triggered as the voltage drops to 0.4 V within a DEA cycle. This purge voltage is chosen to avoid too frequent purges which lead to a waste of hydrogen fuel, and also to avoid extremely low power output. As shown in Subsection 3.1, V_{ap} and t_{cycle} decrease with time, indicating the long-term irreversible degradation, which can be observed in flow-through evaluations including electrochemical diagnosis. As a comparison, the short-term voltage decay within a cycle is due to the nitrogen crossover, which is reversible and can be recovered by purging.

2.3. *Test protocol*

Fig. 3 is a flowchart illustrating the protocol for degradation tests. Initially, the test cell was operated with FTA mode for conditioning, followed by evaluation of beginning-of-life (BOL) performance. The DEA degradation test then started, during which the performance evaluation in FTA mode was performed approximately every 100 h.

In FTA condition, the cell temperature was maintained at 60 °C. Anode and cathode RHs were maintained at 100%, and stoichiometry 1.2 for anode and 2.5 for cathode. The FTA conditions were applied for 10 min to equilibrate the membrane humidification before the polarization evaluation was performed. Current load was scanned from 0 to 0.8 A cm^{-2} twice with a scan rate of 0.08 A s^{-1} to evaluate the i-V performance.

Electrochemical Impedance Spectroscopy (EIS) measurements were also conducted while at FTA condition. The operating conditions were maintained the same as those in i-V evaluation, with 0.2 A cm^{-2} load and a frequency scan from 0.6 Hz to 10 KHz. During the DEA operation, the HFR was recorded together with the voltage data.

Three different cases have been tested as summarized in Table 1. Their difference lies in cell temperature and cathode RH. The dew point for air was maintained at 46 or 60 °C (approximately 50 or 100% in RH) when the cell temperature was at 60 °C. The dew point was 64 °C (approximately 50% in RH) when the cell temperature increased to 80 °C. Throughout the DEA degradation test, the cell was operated with galvanostatic mode (0.4 A cm^{-2} load). The solenoid valve was triggered to purge once the cell voltage reduced to 0.4 V.

In general, each experimental condition (Cases 1–3) targeted 1000-h operating time. However, if apparent MEA failure/damage was observed, then the experiment was stopped before reaching the target time. Rapid voltage drop within a DEA cycle followed by a cell shutdown, and an open circuit voltage (OCV) of 0.9 V or lower, as opposed to the initial value of around 0.96 V, were used as the indicators of MEA failure. Both of these observations indicate a critical membrane failure, typically manifested by pin-holes, at which time the test was stopped. Specifically, Case 1 reached the 1000-h target whereas Cases 2 and 3 halted before reaching 1000 h.

Cyclic voltammetry (CV) using potentiostat (Autolab, Metrohm) was performed to measure the electrochemical surface area (ECSA) at the BOL and EOL (end-of-life), respectively. For this test, nitrogen was used in the cathode (as working/

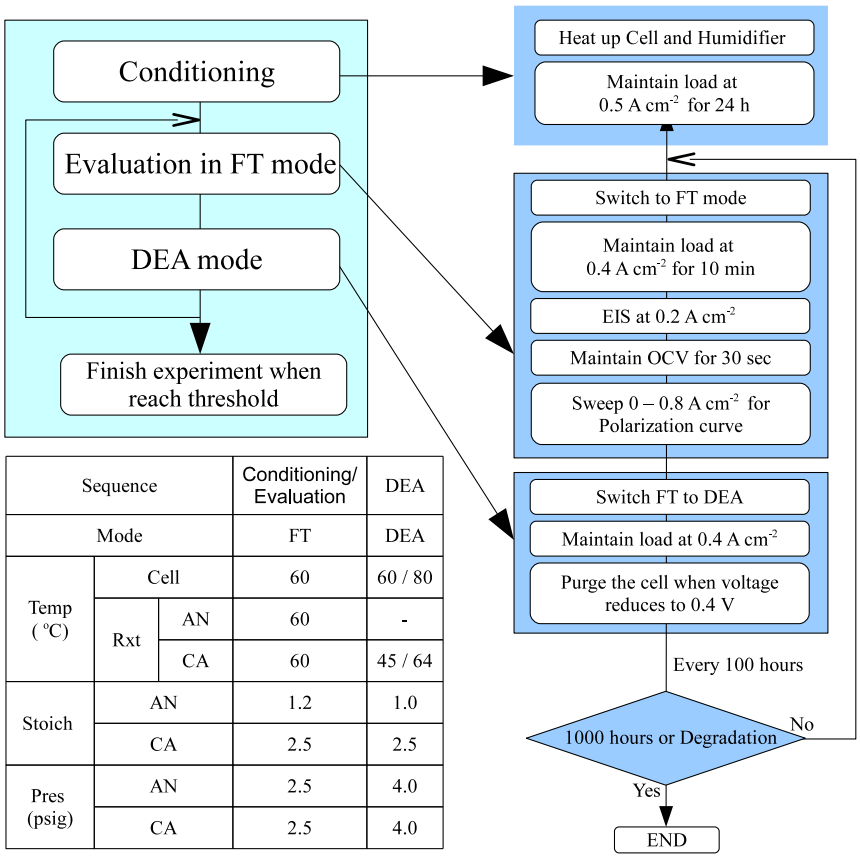

Sequence			Conditioning/ Evaluation	DEA
Mode			FT	DEA
Temp (°C)	Cell		60	60 / 80
	Rxt	AN	60	-
		CA	60	45 / 64
Stoich	AN		1.2	1.0
	CA		2.5	2.5
Pres (psig)	AN		2.5	4.0
	CA		2.5	4.0

Fig. 3 – Flowchart of the experimental protocol.

counter electrode) and hydrogen in the anode (as reference electrode). These gases were supplied at a rate of 0.5 L min^{-1}. The cell was maintained at 23 °C with the same dew point on both sides. The cell was scanned between 0.05 and 0.8 V potential versus reversible hydrogen electrode (RHE) with a rate of 25 mV s^{-1} for three times.

The hydrogen crossover through the membrane is evaluated by linear sweep voltammetry (LSV). During LSV, the cell temperature and dew point were both maintained at 60 °C and a potential from 0.05 to 0.6 V (vs RHE) was applied with a scan rate of 5 mV s^{-1}.

3. Results and discussions

3.1. Cell voltage and resistance

Fig. 4 shows the time evolution of the voltage after each purge V_{ap}, the high frequency resistance (HFR) and the duration of a DEA purge cycle t_{cycle} for each case. The operating conditions are noted in the figure.

In Case 1, which has a cell temperature of 60 °C and cathode relative humidity of 100% as shown in Table 1, the degradation test finished the target time of 1000 h. The cycle duration dropped about 15% compared to the initial cycle duration. Despite the reduced cycle duration, the corresponding OCV values shown in Fig. 5 remained within 1% tolerance of the initial OCV. Under 100% cathode RH, the membrane in Case 1 shows negligible mechanical degradation because the differences in OCV at the BOL and EOL are small. The irreversible voltage loss is most likely due to the catalyst layer degradation verified by the electrochemical diagnostics and SEM imaging in Subsections 3.2 and 3.3.

In Case 2, the cathode relative humidity is 50% and the cell temperature is 60 °C. Initially, t_{cycle} was 37 min. In contrast, this value reduced to about 6 min at the end of the test, with an OCV drop from 0.956 to 0.906 V as shown in Fig. 5. It is very likely that the membrane experienced a pin-hole failure. Due to the low OCV, the degradation test for Case 2 was halted before reaching 1000 h.

In Case 3, which has an elevated cell temperature of 80 °C and 50% cathode RH, the cycle duration decreased from 83 to 17 min and the test lasted only about 400 h. At this time the OCV had decreased from 0.956 to 0.908 and thus the membrane in Case 3 suffered a pin-hole failure as well. The pin-hole failure occurred much earlier in Case 3 than in Case 2.

Table 1 – Operating conditions for DEA degradation tests.

Case	T_{cell} (°C)	T_{hum} (°C)	SR_{CA}(–)	I (A cm^{-2})	RH_{CA}
Case 1	60	60	2.5	0.4	100%
Case 2	60	46	2.5	0.4	50%
Case 3	80	64	2.5	0.4	50%

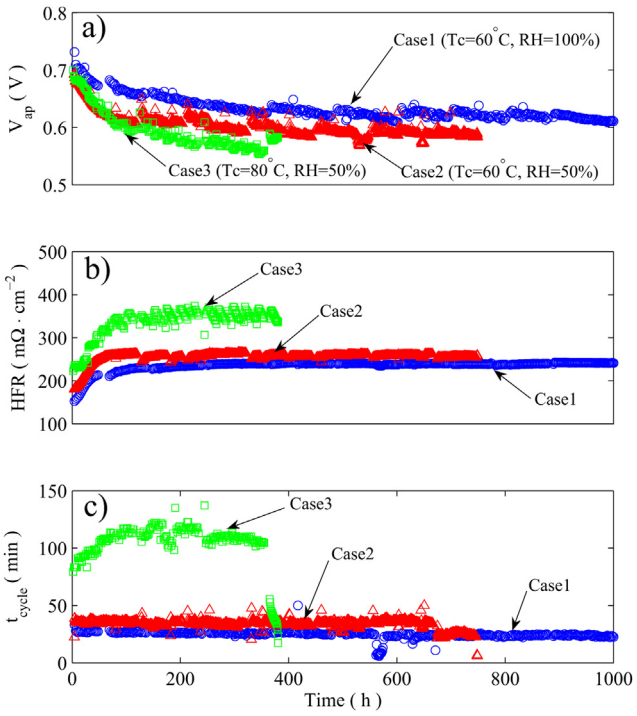

Fig. 4 – Complete data set of three DEA degradation tests with different operating conditions: a) after-purge voltage V_{ap}, b) high frequency resistance, and c) cycle duration t_{cycle}.

It appears that the membrane is more vulnerable under increased temperature, probably due to the more severe inhomogeneity of local current/temperature distribution compared with that under lower cell temperature.

The difference in t_{cycle} between three cases shown in Fig. 4 can be explained by the model of N_2 permeation which is membrane water content (λ) and temperature (T_{cell}) dependent [20]:

$$K_{N_2}(\lambda,\ T_{cell}) = \alpha_{N_2}\left(0.0295 + 1.21f_v - 1.93f_v^2\right) \times 10^{-14} \times \exp\left[\frac{E_{N_2}}{R}\left(\frac{1}{T_{ref}} - \frac{1}{T_{cell}}\right)\right], \quad (1)$$

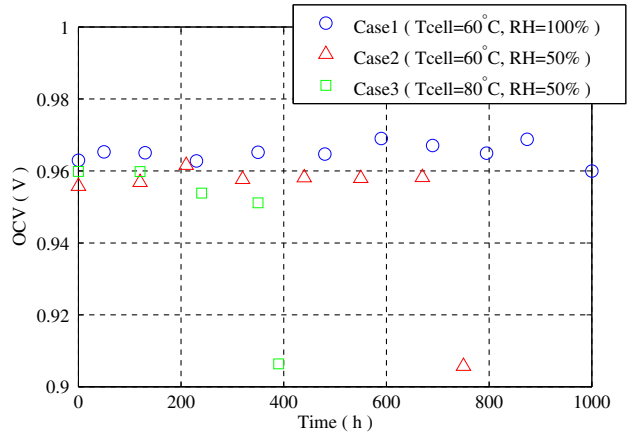

Fig. 5 – The evolution of OCV for three cases.

where α_{N_2} is a tuned scale factor [12], R is the universal gas constant, $E_{N_2} = 24{,}000\ J\ mol^{-1}$, $T_{ref} = 303\ K$, and f_v is the volume fraction of water in the membrane given by:

$$f_v = \frac{\lambda V_w}{V_{mb} + \lambda V_w} \quad (2)$$

where $V_{mb} = EW/\rho_{mb,dry}$ is the dry membrane volume, equivalent weight divided by density, and V_w is the molar volume of water. In Eq. (1), λ can be also expressed as a function of T_{cell} [21]:

$$\lambda = \lambda_{303} + \frac{\lambda_{353} - \lambda_{303}}{50}(T_{cell} - 303) \quad (3)$$

where λ_{303} and λ_{353} are the equilibrium membrane water contents at the temperature of 303 K and 353 K, respectively [22]:

$$\lambda_{303} = 0.043 + 17.81RH - 39.85RH^2 + 36.0RH^3 \quad (4)$$

$$\lambda_{353} = 0.300 + 10.8RH - 16.0RH^2 + 14.1RH^3 \quad (5)$$

where RH indicates the relative humidity of the gas in equilibrium with the membrane. Using Eqs. (1)–(5) one can obtain a functional dependence of K_{N_2} on T_{cell} for different values of RH and λ under equilibrium, as shown in Fig. 6. Increasing T_{cell} from 60 °C to 80 °C with RH = 100% causes a 40% increase of the K_{N_2} value, whereas increasing λ from 4 to 10 approximately doubles the value of K_{N_2}.

For Case 1 in Fig. 6, the cathode inlet condition closely approximates the membrane hydration state, therefore the corresponding N_2 permeabilities from cathode inlet RH and averaged membrane water content are almost the same. However, for Cases 2 and 3, the model [11] predicts different average membrane hydration. From the brown markers indicating the N_2 permeabilities based on the average λ, one can observe that Case 3 shows the smallest N_2 permeability and therefore the largest t_{cycle}.

Fig. 7 presents the spatiotemporal evolutions of the membrane water content, N_2 permeability through the membrane and local current density, obtained by an along-channel model [11] simulation for these three cases. The along-channel distribution of each parameter at three selected times within a cycle is plotted. In the first subplot, the membrane water content in Case 3 is substantially lower than that in the other two cases. Therefore, the average K_{N_2} in Case 3 is the lowest as shown in the second subplot. The local current distribution in the third subplot exhibits large spatial inhomogeneity particularly in Cases 2 and 3, in which the highest local current is observed at the middle region of the channel due to the membrane self-humidification.

In the first 100 h of Fig. 4, HFR increased dramatically, and then it stabilized in all cases. The initial low HFR indicates a high hydration state of membrane after the flow-through conditioning. In DEA operation, there is no humidification for hydrogen. The model predicted membrane drying in the inlet region is shown in the first subplot of Fig. 7. The increasing HFR is due to the gradual drying of the membrane. As the membrane hydration in DEA operation reached equilibrium, HFR stabilized. In Case 3, the high temperature and low RH conditions, which dry the cell, have to be

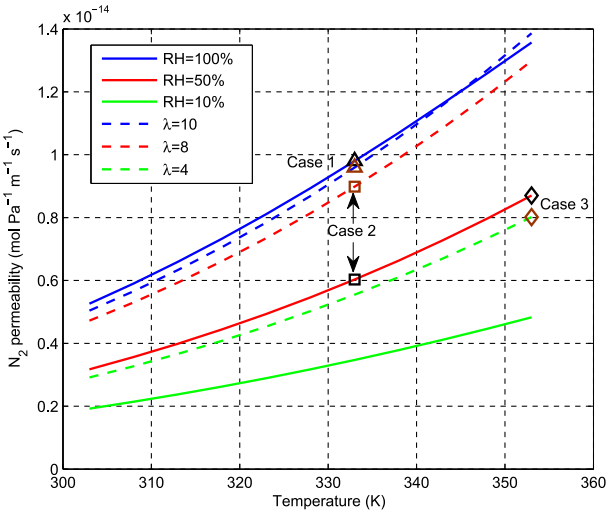

Fig. 6 – The N_2 permeability as a function of T_{cell} for different relative humidities of the gas in equilibrium with the membrane and different membrane water contents. The black markers indicate the corresponding N_2 permeabilities for three degradation test cases based on the cathode relative humidity, whereas the brown markers are based on the average membrane water content. (For interpretation of the references to colour in this figure legend, the reader is referred to the web version of this article.)

achieved before resuming the DEA operation after the diagnostic test. Thus, the HFR in Case 3 does not decrease significantly even right after the flow-through diagnostics every 100 h.

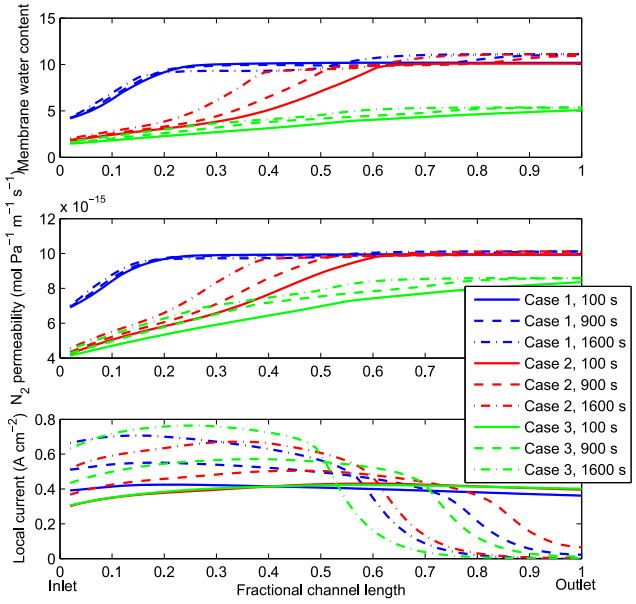

Fig. 7 – The model [11] predicted spatiotemporal evolutions of the membrane water content, N_2 permeability through the membrane and local current density.

3.2. *Electrochemical diagnosis*

Since each case has different operating conditions, it is difficult to compare the degradation effects under DEA condition. Therefore, the periodic performance evaluation in FTA mode was conducted using the following operating conditions: 60 °C cell temperature, 100% RH and 2.5 psig pressure at both anode and cathode, and 1.2 anode stoichiometry and 2.5 cathode stoichiometry as shown in Fig. 3. The FTA diagnostics consisted of EIS (Fig. 9), OCV (Fig. 5) and polarization measurements (Fig. 8). The performance drop in the polarization becomes much smaller after the first diagnostic at BOL, a similar trend observed in Fig. 9.

Fig. 9 shows the Nyquist plots with a frequency range from 10 KHz to 0.6 Hz. Analysis of the EIS results in this paper provides a qualitative understanding of the different overpotentials that contribute to the total voltage loss. In all three cases, the ohmic overpotential increases rapidly in the initial stage (from the first to the second set of diagnostic tests) and then it stabilizes after the second diagnostic tests, as represented by the high frequency intersection. Again, this observation indicates the gradually dried membrane since the DEA operation started after the flow-through conditioning. The similar HFR values after the first diagnostic tests indicate that the chemical degradation of membrane, which increases the cell resistance [23,24], is minor throughout the degradation test, as compared to the major failure, membrane pin-hole, in Cases 2 and 3.

The charge transfer resistance increases throughout the degradation test as represented by the increasing size of the conductive arcs. During the degradation test, the hydrogen starvation, due to the nitrogen blanketing and water accumulation in the anode, led to the cathode carbon corrosion and associated Pt agglomeration [18,25,26]. As a result, the porosity and ECSA of cathode catalyst layer reduced [27,28] and the charge transfer resistance increased.

In Fig. 9, the secondary conductive loops at the low frequency regions are observed for all three cases, which are attributed to the diffusion limitation of oxygen within the catalyst layer [29], suggesting that the cathode stoichiometry ratio in the protocol (Fig. 3) could be further increased while performing EIS measurement. Moreover, the observed low-frequency inductive loops are due to the additional reactions such as the formation of hydrogen peroxide and the formation of PtO with subsequent dissolution of Pt [30], when the cathode local potential was increased during the DEA operation. A recovery step with sufficient idle time appears to be necessary in the protocol before the flow-through evaluation.

The CV measurements at BOL/EOL for all three cases are shown in Fig. 10. The ECSA can be estimated from the hydrogen desorption/adsorption peak by using Eq. (6), in which Q_h indicates the total charge from desorption/adsorption (μC cm^{-2}, integral from the hydrogen adsorption peak). The platinum loading in the electrode in gram is defined as C and S is a constant, representing the single layer saturation coverage for hydrogen on Pt particle surface (210 μC cm^{-2}) [31,32]

$$ECSA\left(cm^2 \cdot g_{Pt}^{-1}\right) = \frac{Q_h(\mu C)}{S(\mu C \cdot cm^{-2}) \cdot C(g_{Pt})} \quad (6)$$

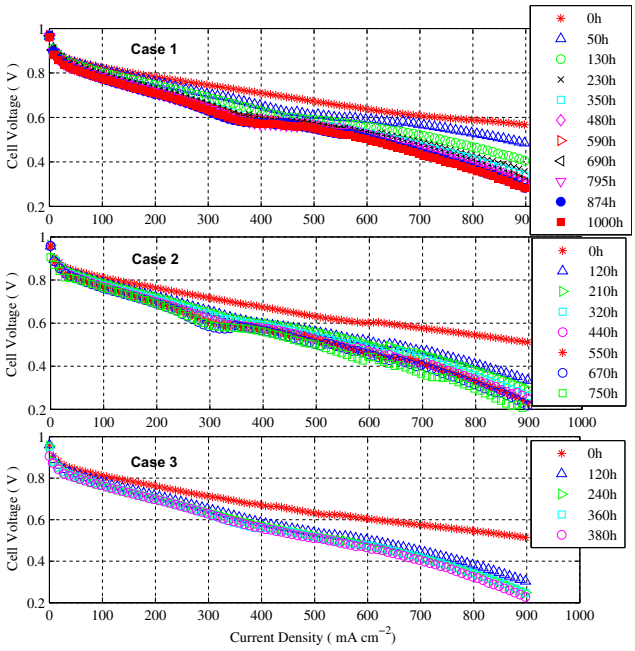

Fig. 8 – The evolution of polarization performance for three cases.

The calculated ECSA is shown in the Table 2. Over 50% of the ECSA has been lost from the initial values for all cases. Although the total test time for Case 3 is much shorter than the other two cases, the ECSA losses are similar in Case 3 and Case 1, indicating that the cathode carbon corrosion accelerates when the temperature increases.

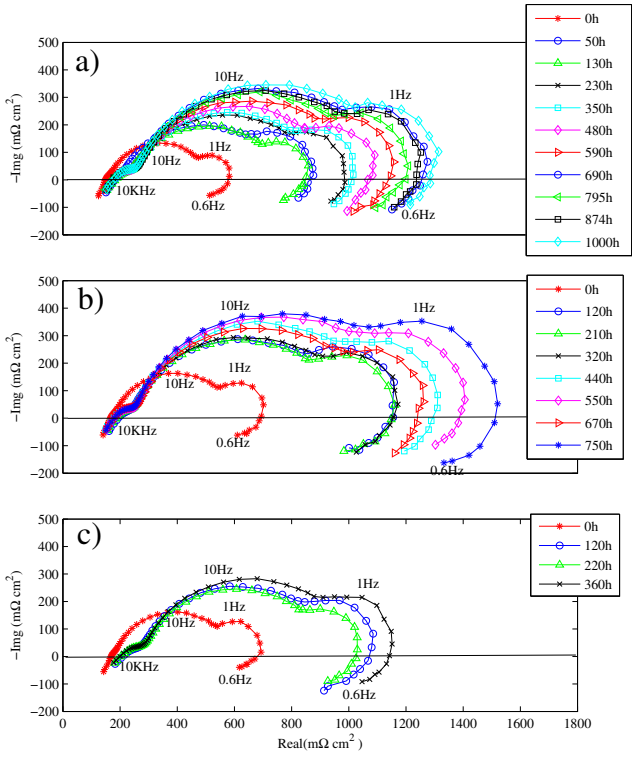

Fig. 9 – Nyquist plots for EIS measurement at 0.2 A cm^{-2}: a) case 1, b) case 2, c) case 3.

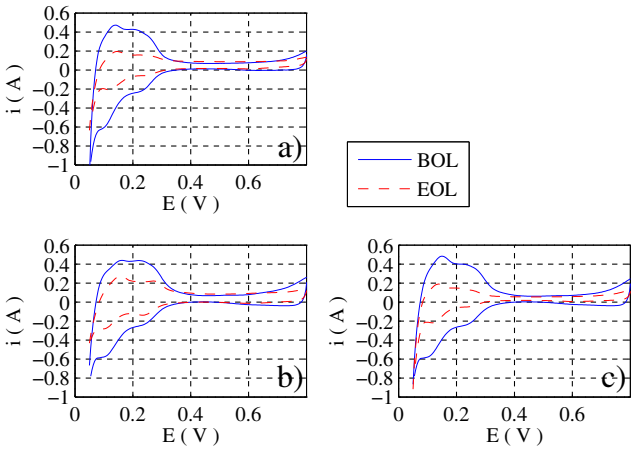

Fig. 10 – CV spectra at BOL/EOL for three cases: a) Case 1, b) Case 2, c) Case 3.

Comparisons of the crossover currents at BOL/EOL by LSV measurements are shown in Fig. 11. The crossover current has similar values at BOL and EOL in Case 1, whereas it increases dramatically at EOL for Cases 2 and 3. This measurement confirms the membrane pin-holes in Cases 2 and 3, as suggested by the OCV results in Fig. 5, which tends to occur at lower cathode RH (50%).

From the electrochemical diagnosis, it can be seen that the cathode catalyst layer experienced continuous degradation due to the hydrogen starvation when approaching the end of a DEA cycle. However, the membrane mechanical failure, usually in a form of pin-hole, could shutdown the cell by dramatically decreasing the voltage within a DEA cycle. The ultimate failure in Cases 2 and 3 was the membrane pin-hole as clearly shown by Fig. 11.

3.3. *SEM imaging*

After the degradation test, the cell was disassembled and the MEA was cut into 25 pieces, as shown in Fig. 1, for SEM imaging. The average thickness of the anode/cathode catalyst layer and electrolyte membrane for each case is summarized in Fig. 12. The first row shows the average thickness of the membrane. The initial membrane thickness was 25–28 μm. The average membrane thickness does not show significant change throughout the degradation test. However, there is localized membrane thinning in the cell inlet region that will be shown in Fig. 14.

The average thickness of the cathode catalyst layer is presented in the second row of Fig. 12. The fresh catalyst layer has a thickness of 14–16 μm for both anode and cathode.

Table 2 – The calculated cathode ECSA at BOL/EOL for three cases.

	Case 1	Case 2	Case 3
BOL ECSA ($cm^2 g_{Pt}^{-1}$)	7.919×10^5	7.360×10^5	7.407×10^5
EOL ECSA ($cm^2 g_{Pt}^{-1}$)	2.863×10^5	3.744×10^5	2.7454×10^5

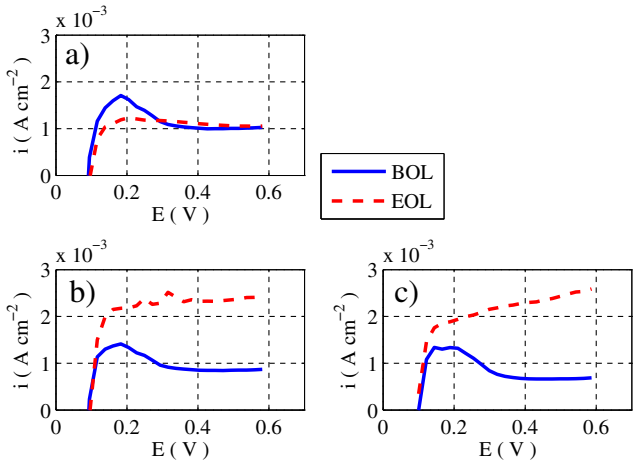

Fig. 11 – LSV spectra at BOL/EOL for all cases: a) Case 1, b) Case 2, c) Case 3.

There is a large difference in the cathode catalyst layer thickness from the inlet to the outlet, and the variation trend is similar for all cases. At the hydrogen inlet region (column A, see Fig. 1), the cathode catalyst layer shows similar thickness as compared to the fresh one, whereas the catalyst layer at the end region (column E) exhibits 50–70% loss of thickness after the degradation test in all cases. Indeed, carbon corrosion is significant only in the cathode regions with hydrogen starvation in the opposite anode. The thickness of the anode catalyst layer did not change after the degradation test in Cases 1 and 2 due to the low anode potential and negligible amount of carbon corrosion.

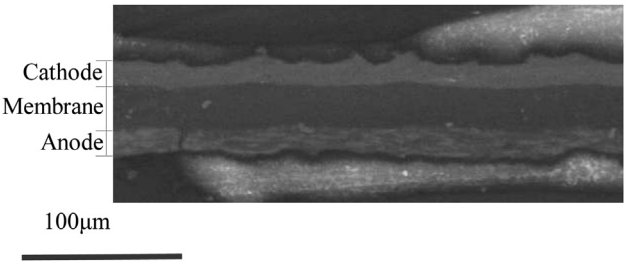

Fig. 13 – SEM image of the MEA cross section at BOL.

In addition to reporting the average thickness, representative SEM images showing the MEA cross sections are presented in Figs. 13–15. The BOL MEA is shown in Fig. 13; both the membrane and catalyst layer are homogeneous. In Fig. 14, localized membrane thinning is observed in Cases 2 and 3 at the inlet region, although the average thickness changes slightly.

In all cases, the model predicts low membrane water content at the inlet region, as well as a large temporal variation of the local current at the inlet and middle channel regions within a DEA cycle, as illustrated by Fig. 7. Furthermore, in Case 2, there also exists substantial magnitude of membrane water content cycling in the middle channel region as shown in the first subplot of Fig. 7. The additional mechanical stress introduced by these dry and cycling conditions is responsible for the

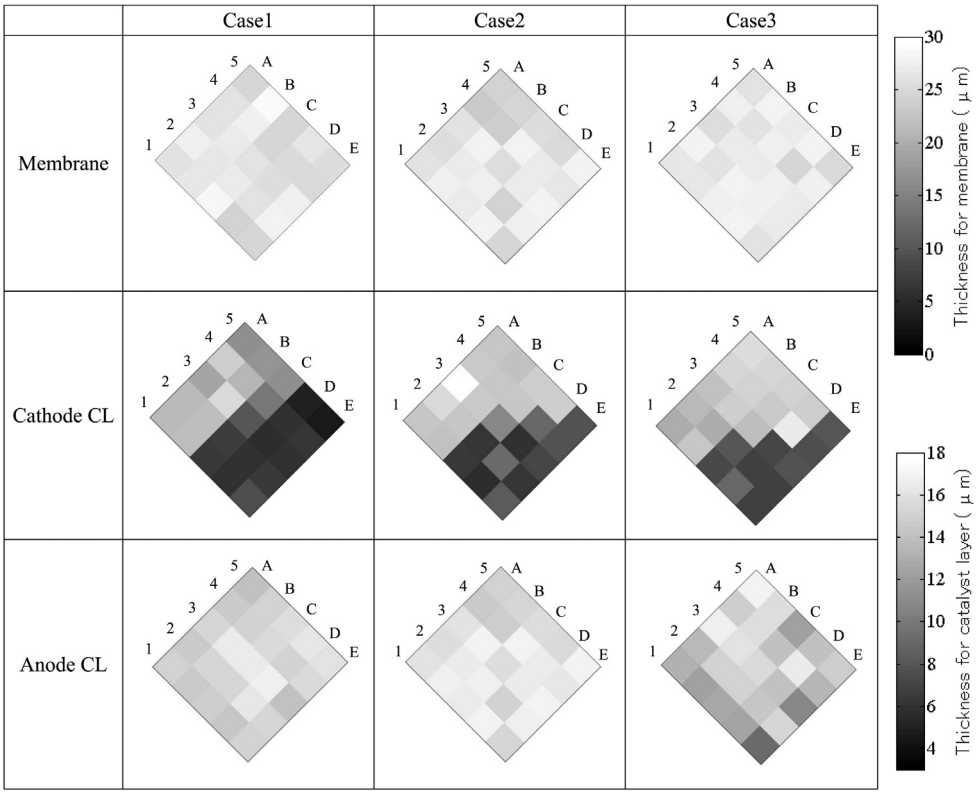

Fig. 12 – The thickness of MEA components (membrane and cathode/anode catalyst layer): the upper color bar is the gauge for membrane, and the bottom one for catalyst layer.

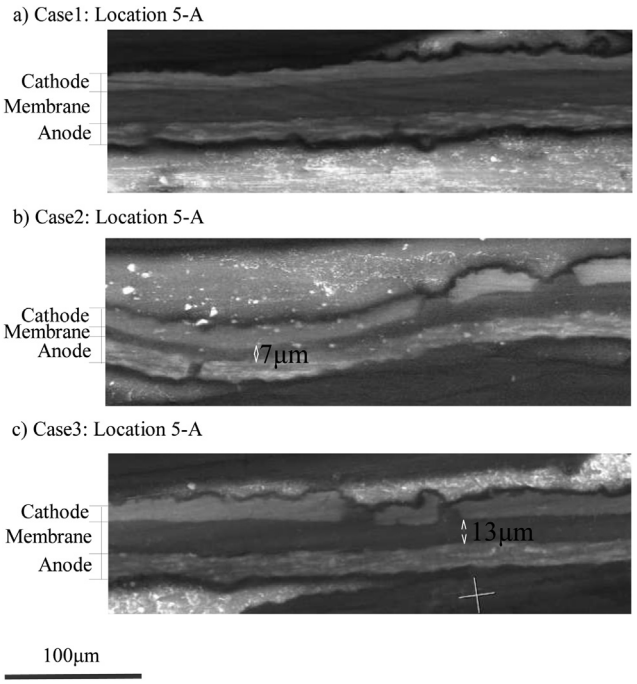

Fig. 14 – SEM image of the MEA cross section showing localized membrane thinning at the inlet.

local thinning of the membrane in Cases 2 and 3, as well as the severe membrane delamination as shown in Fig. 15. This style of damage closely resembles the failure when the cell is tested under dry/wet or freeze/thaw cycles [33–35]. Generally, the inadequate water content, uneven local stress and current, and cycling operation are the culprits for accelerated mechanical degradations [36].

The continuous supply with 100% RH in the cathode in Case 1 appears to alleviate the mechanical stress from the

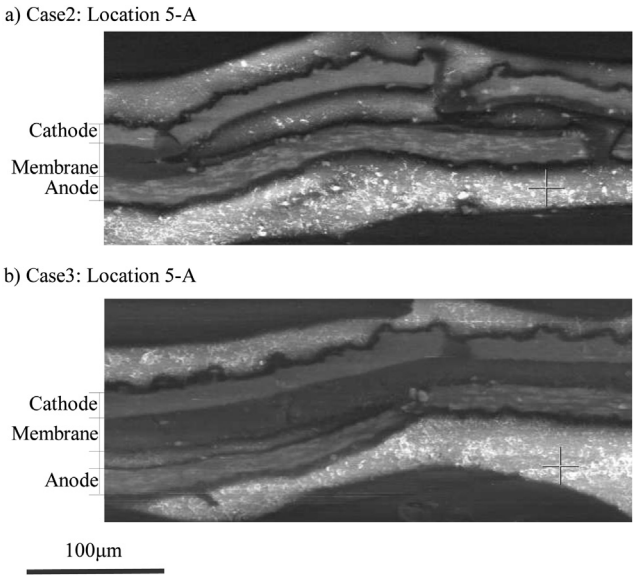

Fig. 15 – SEM image of the MEA cross section showing membrane delamination and catalyst layer damage at the inlet.

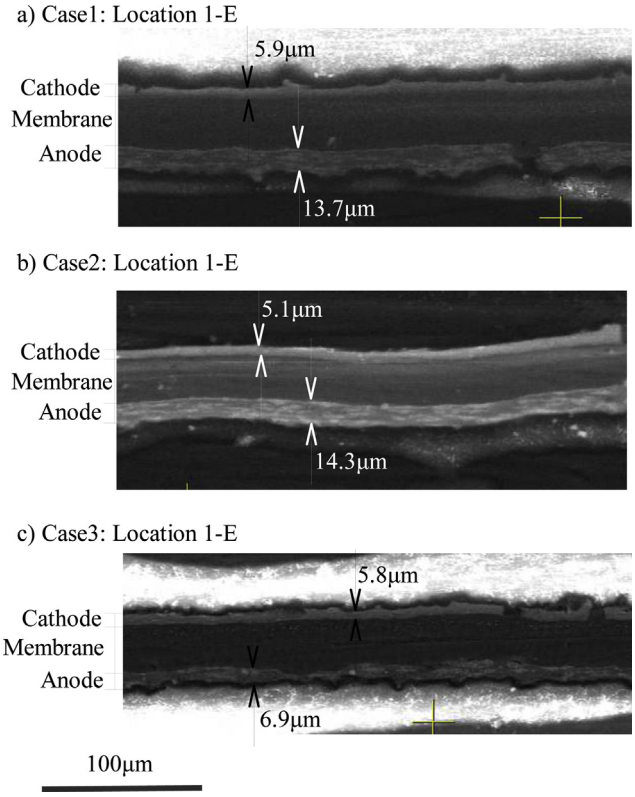

Fig. 16 – SEM image of the MEA cross section showing catalyst layer thinning at the outlet.

cycling conditions, since the postmortem membrane was generally homogeneous without localized thinning from the SEM imaging. The model also predicts that in Case 1, the membrane water contents in the inlet and middle channel regions remain at a high level within a DEA cycle, as shown in the first subplot of Fig. 7.

In Fig. 16, the thinning of the cathode catalyst layer can be clearly seen for all cases. It is interesting to observe the anode catalyst layer thinning in Case 3. Higher temperature may reduce the thermodynamic equilibrium voltage for carbon and accelerate the rate of carbon corrosion. Further experimental study is needed to validate this finding.

4. Conclusions

The degradation phenomena in DEA operation of a PEMFC have been experimentally investigated for three cases with different cell temperatures and cathode supply RHs. Both membrane and catalyst layer degradations were observed from the in-situ electrochemical diagnosis and SEM imaging of the aged MEA samples. The ultimate failure in the degradation test was the membrane pin-hole, which occurred under low cathode RH (50%), as shown by the crossover current and OCV measurements. Once the pin-hole formed, the voltage dramatically decreased within a DEA cycle and the cell shutdown. Therefore, only Case 1 with 100% cathode supply RH completed 1000 h of DEA operation, whereas Cases 2 and 3 were halted due to the pin-hole failure. Cathode carbon corrosion due to the anode

hydrogen starvation leads to gradual and continuous degradation of cell voltage throughout the DEA operation, which is confirmed by the increasing charge transfer resistance from the EIS, the decreasing ECSA from the CV, and the catalyst layer thinning from the SEM imaging.

Although the average membrane thickness shows small change throughout the degradation test, local membrane thinning and delamination have been observed due to the dry conditions in the inlet region. The membrane chemical degradation appears to be minor throughout the test because the HFR showed small variation. Longer DEA operation beyond 1000 h is probably necessary to identify the influence from the chemical degradation. With a reinforced membrane that can prevent pin-hole failure from interrupting the degradation test, the chemical degradation under DEA condition will be investigated in the future.

Acknowledgments

This work is funded by the National Science Foundation through CBET-0932509 and Ford Motor Company.

REFERENCES

[1] Ahluwalia R, Wang X. Fuel cell systems for transportation: status and trends. Journal of Power Sources 2008;177(1):167–76.
[2] Bose S, Kuila T, Nguyen T, Kim N, Lau K, Lee J. Polymer membranes for high temperature proton exchange membrane fuel cell: recent advances and challenges. Progress in Polymer Science 2011;36(6):813–43.
[3] Park C, Lee C, Guiver M, Lee Y. Sulfonated hydrocarbon membranes for medium-temperature and low-humidity proton exchange membrane fuel cells (PEMFCs). Progress in Polymer Science 2011;36(11):1443–98.
[4] Prabhuram J, Krishnan N, Choi B, Lim T, Ha H, Kim S. Long-term durability test for direct methanol fuel cell made of hydrocarbon membrane. International Journal of Hydrogen Energy 2010;35(13):6924–33.
[5] Sethuraman V, Weidner J, Haug A, Protsailo L. Durability of perfluorosulfonic acid and hydrocarbon membranes: effect of humidity and temperature. Journal of The Electrochemical Society 2008;155:B119.
[6] Cavarroc M, Ennadjaoui A, Mougenot M, Brault P, Escalier R, Tessier Y, et al. Performance of plasma sputtered fuel cell electrodes with ultra-low Pt loadings. Electrochemistry Communications 2009;11(4):859–61.
[7] Olson T, Chapman K, Atanassov P. Non-platinum cathode catalyst layer composition for single membrane electrode assembly proton exchange membrane fuel cell. Journal of Power Sources 2008;183(2):557–63.
[8] Rodatz P, Büchi F, Onder C, Guzzella L. Operational aspects of a large PEFC stack under practical conditions. Journal of Power Sources 2004;128(2):208–17.
[9] Mocoteguy P, Druart F, Bultel Y, Besse S, Rakotondrainibe A. Monodimensional modeling and experimental study of the dynamic behavior of proton exchange membrane fuel cell stack operating in dead-end mode. Journal of Power Sources 2007;167:349–57.
[10] McKay D, Siegel J, Ott W, Stefanopoulou A. Parameterization and prediction of temporal fuel cell voltage behavior during flooding and drying conditions. Journal of Power Sources 2008;178:207–22.
[11] Chen J, Siegel J, Stefanopoulou A, Waldecker J. Optimization of purge cycle for dead-ended anode fuel cell operation. International Journal of Hydrogen Energy 2013;38:5092–105.
[12] Siegel J, Bohac S, Stefanopoulou A, Yesilyurt S. Nitrogen front evolution in purged polymer electrolyte membrane fuel cell with dead-ended anode. Journal of The Electrochemical Society 2010;157:B1081.
[13] Siegel J, McKay D, Stefanopoulou A, Hussey D, Jacobson D. Measurement of liquid water accumulation in a PEMFC with dead-ended anode. Journal of The Electrochemical Society 2008;155:B1168.
[14] Patterson T, Darling R. Damage to the cathode catalyst of a pem fuel cell caused by localized fuel starvation. Electrochemical and Solid-state Letters 2006;9(4):A183–5.
[15] Liu Z, Brady B, Carter R, Litteer B, Budinski M, Hyun J, et al. Characterization of carbon corrosion-induced structural damage of PEM fuel cell cathode electrodes caused by local fuel starvation. Journal of The Electrochemical Society 2008;155(10):B979–84.
[16] Baumgartner W, Parz P, Fraser S, Wallnofer E, Hacker V. Polarization study of a PEMFC with four reference electrodes at hydrogen starvation conditions. Journal of Power Sources 2008;182(2):413–21.
[17] Liang D, Shen Q, Hou M, Shao Z, Yi B. Study of the cell reversal process of large area proton exchange membrane fuel cells under fuel starvation. Journal of Power Sources 2009;194(2):847–53.
[18] Chen J, Siegel J, Matsuura T, Stefanopoulou A. Carbon corrosion in PEM fuel cell dead-ended anode operations. Journal of The Electrochemical Society 2011;158(9):B1164–74.
[19] Matsuura T, Siegel J, Chen J, Stefanopoulou A. Multiple degradation phenomena in polymer electrolyte fuel cell operation with dead-ended anode. In: Proceedings of the ASME 2011 9th international conference on fuel cell Science, engineering and technology 2011. p. 127–35.
[20] Ahluwalia R, Wang X. Buildup of nitrogen in direct hydrogen polymer-electrolyte fuel cell stacks. Journal of Power Sources 2007;171(1):63–71.
[21] Ge S, Li X, Yi B, Hsing I-M. Absorption, desorption, and transport of water in polymer electrolyte membranes for fuel cells. Journal of the Electrochemical Society 2005;152:A1149–57.
[22] Springer TE, Zawodzinski TA, Gottesfeld S. Polymer electrolyte fuel cell model. Journal of The Electrochemical Society 1991;138:2334–42.
[23] Kinumoto T, Inaba M, Nakayama Y, Ogata K, Umebayashi R, Tasaka A, et al. Durability of perfluorinated ionomer membrane against hydrogen peroxide. Journal of Power Sources 2006;158(2):1222–8.
[24] Mittal V, Kunz H, Fenton J. Membrane degradation mechanisms in PEMFCs. Journal of The Electrochemical Society 2007;154:B652–6.
[25] Reiser C, Bregoli L, Patterson T, Jung S, Yang J, Perry M, et al. A reverse-current decay mechanism for fuel cells. Electrochemical and Solid-State Letters 2005;8(6):A273–6.
[26] Ohs J, Sauter U, Maass S, Stolten D. Modeling hydrogen starvation conditions in proton-exchange membrane fuel cells. Journal of Power Sources 2011;196(1):255–63.
[27] Cherstiouk O, Simonov A, Moseva N, Cherepanova S, Simonov P, Zaikovskii V, et al. Microstructure effects on the electrochemical corrosion of carbon materials and carbon-supported Pt catalysts. Electrichimita Acta 2010;55:8453–60.
[28] Artyushkov K, Pylypenko S, Dowlapalli M, Atanassov P. Structure-to-property relationships in fuel cell catalyst supports: correlation of surface chemistry and morphology with oxidation resistance of carbon blacks. Journal of Power Sources 2012;214:303–13.

[29] Bultel Y, Genies L, Antoine O, Ozil P, Durand R. Modeling impedance diagrams of active layers in gas diffusion electrodes: diffusion, ohmic drop effects and multistep reactions. Journal of Electroanalytical Chemistry 2002;527:143–55.
[30] Roy SK, Orazem ME, Tribollet B. Interpretation of low-frequency inductive loops in PEM fuel cells. Journal of the Electrochemical Society 2007;154:B1378–88.
[31] Green C, Kucernak A. Determination of the platinum and ruthenium surface areas in platinum-ruthenium alloy electrocatalysts by underpotential deposition of copper. i. unsupported catalysts. The Journal of Physical Chemistry B 2002;106(5):1036–47.
[32] Pozio A, De Francesco M, Cemmi A, Cardellini F, Giorgi L. Comparison of high surface Pt/C catalysts by cyclic voltammetry. Journal of Power Sources 2002;105(1):13–9.
[33] Lim S, Park G, Park J, Sohn Y, Yim S, Yang T, et al. Investigation of freeze/thaw durability in polymer electrolyte fuel cells. International Journal of Hydrogen Energy 2010;35(23):13 111–113 117.
[34] Kang J, Kim J. Membrane electrode assembly degradation by dry/wet gas on a PEM fuel cell. International Journal of Hydrogen Energy 2010;35(23):13 125–13 130.
[35] Kim S, Khandelwal M, Chacko C, Mench M. Investigation of the impact of interfacial delamination on polymer electrolyte fuel cell performance. Journal of The Electrochemical Society 2009;156(1):B99–108.
[36] Wu J, Yuan XZ, Martina JJ, Wang H, Zhang J, Shen J, et al. A review of PEM fuel cell durability: degradation mechanisms and mitigation strategies. Journal of Power Sources 2008;184:104–19.